Supplementary Material

Yb/Ho co-doping and rGO bridging enhance visible-to-NIR-light driven photocatalysis in an S-scheme Heterojunction

Piaopiao Wu[a], LiJia Xie[a], Weiya Huang[a,*], Liqing Li[a], Kai Yang[a], Xianqiang Xiong[b,c*]

a. School of Chemistry and Chemical Engineering, Jiangxi University of Science and Technology, Ganzhou, 341000, PR China

b. Zhejiang Key Laboratory for Island Green Energy and New Materials, Taizhou University, Taizhou, 318000, P.R. China

c. Taizhou Biomedical and Chemistry Industry Institute, Taizhou 31800, P.R. China

*Corresponding author:

E-mail addresses: hweiya@126.com (W-Y. Huang); 11337061@zju.edu.cn (X. Q. Xiong)

Section A. Materials and methods

S1. Chemicals

Nickel nitrate ($Ni(NO_3)_2·6H_2O$), ferric nitrate ($Fe(NO_3)_3·9H_2O$), yttrium nitrate ($Yb(NO_3)_3·6H_2O$), holmium nitrate ($Ho(NO_3)_3·6H_2O$), ammonium fluoride (NH_4F) and urea ($CO(NH_2)_2$), hydrochloric acid (HCl) were purchased from Xilong Scientific Co., Ltd (Guangdong, China). Thioacetamide(C_2H_5NS) was purchased from Macklin Biochemical Co., Ltd (Shanghai, China). Graphite powder, Indium nitrate tetrahydrate(($InNO_3)_3·4H_2O$) was purchased from Aladdin Biochemical Technology Co., LTD (Shanghai, China).

S2. Synthesis methods

Synthesis of GO

The preparation of graphene oxide (GO) is carried out by the improved Hummers chemical oxidation synthesis method. 2g of graphite powder is added to 46 mL of concentrated sulfuric acid and placed in an ice water bath. Slowly pour in 6 g of $KMnO_4$, mix evenly without releasing heat, then heat the water bath to 35°C and stir for 2 hours. Add 400 mL of deionized water. 16 mL H_2O_2. Add the hydrochloric acid solution diluted ten times and centrifuge and wash three times at 7000 r/min. After dialysis for one week, vacuum dry at 60°C for three days to obtain the film-like GO.

Synthesis of Yb and Ho co-doped NiFe LDH

1.45 g $Ni(NO_3)_2·6H_2O$, 1.01 g $Fe(NO_3)3·9H_2O$, 0.089 g $Yb(NO_3)_3·5H_2O$ and a certain amount of $Ho(NO_3)_3·5H_2O$ (0.011 g, 0.033 g, 0.055 g) were dissolved in 25 mL deionized water (denoted as A). Dissolve 0.005 mol Na_2CO_3 and 0.015 mol NaOH in 25 mL of deionized water (marked B). Under magnetic stirring, the mixed metal solution and alkaline solution are simultaneously dropped into 25 mL of deionized water (marked as C), and the pH value of the whole process is monitored to be 10 ± 0.5. The grey suspension was stirred continuously for 4 hours and subsequently aged in an oil bath at 80°C for 2 hours. The sample was washed 3 times with deionized water and absolute ethanol and dried under vacuum at 60°C for 24 hours (the actual yield of NiFe LDH was about 0.8 g). The resulting sample was named xHo 8Yb-LDH (x = 1, 3, 5). The best sample 3Ho8Yb-LDH named YH-NF. Meanwhile, pure NiFe LDH was prepared by the same method except that rare earth was not added in the preparation process.

Synthesis of YH-NF/rGO

YH-NF/xrGO was prepared by the same procedure as YH-NF except that solution C was replaced by an aqueous solution containing GO (40 mg, 80 mg, 160 mg) dispersed therein. The resulting sample was named YH-NF/zrGO(z = 5, 10, 20).The best sample YH-NF/10rGO named YH-NF/rGO.

Synthesis of Yb, Ho-NiFe LDH/In_2S_3 and Yb and Ho-NiFe LDH/rGO

0.11 g YH-NF/rGO was ultrasonically dispersed in 50 mL deionized water, 0.203, 0.41, 0.81 g $(InNO_3)_3{\cdot}4H_2O$ were added, stirred for 90 min, 0.12, 0.24, 0.48 g thioacetamide (TAA) was added, stirred for 10 min, and heated to reflux in an oil bath at 95°C for 6 h. After cooling to room temperature, the sample was washed by centrifugation with deionized water and ethanol for 3 times, dried under vacuum at 60°C for 24 h, and named YH-NF/rGO/ISy (y = 0.5, 1, 1.5). The sample YH-NF/rGO/IS_1 is named YH-NF/rGO/IS for short.

Section B. Characteristics

The X-ray diffraction (XRD) patterns were recorded using the Bruker D8-Advance X-ray powder diffraction instrument with Cu Ka radiation (λ = 0.15418 nm). The morphology and surface composition structure were characterized by a scanning electron microscope (SEM, FEI Quanta 250) and a transmission electron microscope (TEM, FEI Tecnai G220). The chemical compositions of obtained samples were analyzed by an X-ray photoelectron spectroscopy (XPS, Thermo Scientific K-Alpha). The specific surface areas of samples were measured by a nitrogen adsorption analyzer (Micromeritics ASAP 2020). The Fourier transform infrared (FT-IR) spectra were recorded on a Nicolet 5700 FT-IR spectrometer. The UV-Vis-NIR diffuse reflectance spectra (DRS) were recorded with a UV–Vis spectrophotometer (Shimadzu UV-3600i Plus) in the range of 200-1200 nm. Before collecting sample data, a baseline scan was performed using a barium sulfate standard whiteboard. Once calibration is finished, position the sample for testing on the designated side and proceed to gather its spectrum. The electron spin resonance (ESR) spectra were recorded on an electron spin resonance spectrometer (Bruker A300) with 5,5-dimethyl-1-pyrroline Noxide (DMPO: 50 mM, 0.2 mL). The electrochemical measurements of samples were performed on an electrochemical workstation with a standard three-electrode system (Shanghai Chenhua, CHI 760E) and a 300 W Xe lamp (PLS-SXE300, Perfect Light Company, Beijing, China) as the light source. Time-resolved fluorescence decay spectra of samples were recorded on a fluorescence spectrometer (Hitachi F7100).

Nitrate ion chromatography was recorded with a Thermo scientific DIONEX AQUION RFIC

(United States, ICS-6000). Prepare standard solutions by diluting the stock to a concentration series, then construct a calibration curve with mass concentration as the abscissa and peak area/height as the ordinate. Inject standards in increasing concentration and record the responses. Analyze samples under the same chromatographic conditions. Identify anions by retention time and quantify using the instrument response. If the response exceeds the calibration range, dilute the sample appropriately (typically 50–100× prior to injection) and re-analyze. Record the dilution factor (f). Also analyze a blank sample under identical conditions for background correction.

KPFM were recorded with a Bruker Dimension ICON (United States). Xenon lamp was use as light source and a light intensity of 1000W/m^2 was applied for irradiation. The work function of the KPFM tip is calibrated to be 4.42 eV with highly oriented pyrolytic graphite.

XPS measurements were carried out using the ESCALAB 250Xi X-ray photoelectron spectroscopy instrument from Thermo Fisher Scientific. The system was excited using a monochromatic aluminum Kα X-ray source (1486.6 electron volts) and the working environment was at room temperature. The light source was provided by a 300-watt xenon lamp (PLS-SXE300E, Beijing Perfect Light, China), with the emitted light wavelength range exceeding 420. Before conducting the irradiation experiment, XPS spectra of all elemental components in the sample were collected in the dark state as reference data. The charging effect was corrected by setting the C 1s binding energy of the external carbon to 284.8 electron volts. Related parameters: Type of radiation source: Monochromatic Al target (E = 1486.68 eV); Voltage: 14.8 KV; Current: 9.2 mA; Vacuum: <10^{-9} mbar; Work Function: 4.42 eV; Xenon lamp model: Beijing Perfectlight Technology Co., Ltd. PLS-SXE300E (300 W); The acquisition time (20 min).

Section C. Photocatalytic performances

To evaluate the photocatalytic performances of the samples, the decomposition of ONP under visible/near infrared light irradiation was tested. A 300 W xenon lamp (PLS-SXE300, PerfectLight Company, Beijing, China) with a 420 or a 980 nm cut-off filter was used to simulate visible light or + near infrared (NIR) light. When performing the simulated visible + NIR light experiments, the lamp power is set to 1.5 W; when performing the NIR light experiments, the lamp power is set to 1.2 W. The specifications of the filters are 59 mm in diameter and 2 mm in thickness. In visible experiments, the average light power density measures 555.56 W/m^2 (λ≥420), whereas for NIR experiments, it is

recorded at 444.45 W/m^2 (λ≥980). O-nitrophenol (ONP) and tetracycline hydrochloride (TC) were chosen as the model pollutants to prepare wastewater. Typically, 20-60 mg of the catalyst was dispersed in a quartz reactor containing 50 mL ONP with an initial concentration of 10 or 20 mg/L. The resulting suspension was stirred in the dark for 60 min to reach the adsorption–desorption equilibrium of ONP over the catalyst, before exposure to the simulated visible light for another 60 min. During the reaction process, 3 mL of the suspension was sampled at regular intervals and then centrifuged to remove the catalyst. The residual ONP in the supernatant was analyzed by a UV–Vis spectrophotometer (UV-8000, Metash Instrument Co. Ltd., Shanghai, China) at the wavelength of 278 nm. The trapping experiments were carried out by using p-benzoquinone (p-BQ), disodium ethylenediaminetetraacetate (EDTA-2Na), β-carotene and tert-butanol (TBA) as scavengers for superoxide radical ($\cdot O_2^-$), holes (h^+), $^1O_2$ and hydroxyl radical (·OH), respectively.

The effects of common coexisting anions on the photocatalytic performance of the optimal sample YH-NF/rGO/IS were investigated by adding 0.01 mol/L of Na_2SO_4, NaCl, $NaNO_3$ and NaF to the pollutant solution. In the cyclic experiments, all the experimental processes were consistent with the catalytic effect tests. After each cycle, the catalyst is filtered out of the reaction solution and washed with deionized washing water. Then the catalyst is dried in a vacuum oven before proceeding to the next experimental cycle.

Section D Data analysis and fitting

Photoelectrochemistry (PEC)

The PEC performance of NiFe LDH, IS, and YH-NF/rGO/IS was studied using a conventional three-electrode cell on an electrochemical workstation (Shanghai Chenhua Chi 760E). The exposed area of the working electrode was 1×1 cm², the catalyst loading was 10 mg, and the thickness was 1 mm. The working electrode was prepared using 10wt % naphthol as the binder. The saturated Ag/AgCl electrode was used as the reference electrode, the carbon rod as the counter electrode, and the xenon lamp with a filter (λ>420 nm) was used to simulate visible light. The charge transfer kinetics of the catalyst was studied in a 0.2 M Na_2SO_4 solution (pH=7).

The bandgap (E_g) of the semiconductor is calculated according to the Tauc **Equation S1**:

$$\alpha h\nu = A\left(h\nu - E_g\right)^{\frac{n}{2}} \qquad \text{S1}$$

Where, α is the absorption coefficient, hν is the energy of the absorbed photon, and A is a proportional constant. The value of n, the exponent, depends on the type of semiconductor.

The valence band (VB) of semiconductor is calculated according to the **Equation S2**

$$E_{VB,NHE} = \varphi + E_{VB-XPS} - 0.44\ eV \quad \text{S2}$$

Where ϕ is the working function of the XPS analyzer .

Degradation rate $$\eta = \frac{C_0 - C_t}{C_0} \times 100\% \quad \text{S3}$$

First-order kinetic equation $$ln(C/C_0) = -kt \quad \text{S4}$$

Among them, η is the degradation rate, C_0 is the initial concentration of the pollutant, C_t is the concentration of the pollutant at different times, and k is the apparent reaction rate constant .

The contribution of different capture agents to ONP degradation is estimated by the following **Equations S5-8** :

$$R_{\cdot O_2^-} = \frac{k_{\cdot O_2^-}}{k_0} = \frac{k_0 - k_{p-BQ}}{k_0} \quad \text{S5}$$

$$R_{\cdot OH} = \frac{k_{\cdot OH}}{k_0} = \frac{k_0 - k_{TBA}}{k_0} \quad \text{S6}$$

$$R_{^1O_2} = \frac{k_{^1O_2}}{k_0} = \frac{k_0 - k_{CAR}}{k_0} \quad \text{S7}$$

$$R_{h^+} = \frac{k_{h^+}}{k_0} = \frac{k_0 - k_{EDTA}}{k_0} \quad \text{S8}$$

Where R is the contribution ratio of a specific reactant species; ki are the reaction rate constants of $\cdot O_2^-$, $\cdot OH$, $^1O_2$, and h^+ in the presence of PBQ, TBA, Carotene, and EDTA-2Na, respectively; K_0 is the reaction rate constant of ONP without any scavengers. In addition, the contribution percentages need to be normalized.

The relevant calculations for KPFM are as follows:

$$V_{CPD} = V_{sample} - V_{tip} = \frac{W_{tip} - W_{sample}}{e} \quad \text{S9}$$

$$E_f = -W \quad \text{S10}$$

Surface photovoltage (SPV) $= \mathbf{V_{CPD-light} - V_{CPD-dark}}$ S11

where V_{CPD} stands for the contact potential difference between the sample and tip, while V_{sample} and V_{tip} are the absolute potentials of the sample and probe, respectively. In addition, W_{tip} and W_{sample} denote the work functions of the tip and sample, respectively[4]. the values of $V_{CPD\text{-}dark}$ and $V_{CPD\text{-}light}$ refers to the difference between the V_{CPD} in the dark and the V_{CPD} under illumination.

Section E. Density functional theory (DFT) calculations

Spin polarized DFT calculations were performed using the Quantum ESPRESSO package[5, 6]. The exchange-correlation functional was described by the PBE generalized gradient approximation[7, 8], and dispersion interactions were included using the DFT-D3 correction as implemented in QE[9, 10]. Core-valence interactions were modeled using Ultrasoft Pseudopotentials (USPP) from the Standard Solid State Pseudopotentials Efficiency library.

The kinetic energy cutoffs for wavefunctions and charge density were set to 40 Ry and 320 Ry, respectively, ensuring robust numerical convergence. To account for the strong correlation of 3d electrons, the DFT+U method was applied with effective Hubbard parameters of UeffFe = 5.3 eV and UeffNi = 6.2 eV[11].

The surface model was built from a NiOOH (001) slab in which 1/4 of the Ni sites were substituted by Fe to represent the NiFe LDH model consistent with prior work. The slab contained 4 atomic layers with a vacuum thickness of 15 Å along the z direction. A dipole correction along z was included to remove spurious electric fields across the vacuum region.

Brillouin zone sampling used a Monkhorst Pack k point grid of 3×3×1. Geometry relaxations were performed using the BFGS quasi Newton algorithm until the residual forces were below 1×10^{-3} Ry/Bohr and the total energy change was below 1×10^{-4} Ry. A Gaussian smearing width of 0.01 Ry was used to aid electronic convergence.

The work function was calculated as $\Phi = E_{vac} - EF$, where E_F is the Fermi energy from the self-consistent calculation, and E_{vac} is the vacuum potential level, determined from the plateau of the planar-averaged electrostatic potential along the surface normal[12].

Section F. Figures

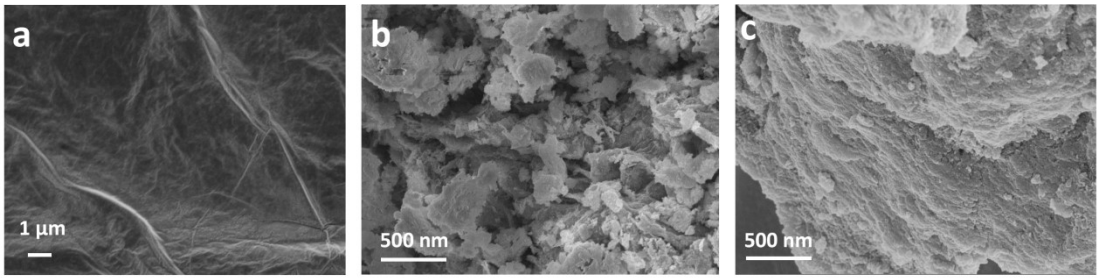

Fig. S1 SEM images of (a) GO, (b) IS, and (c) NiFe LDH.

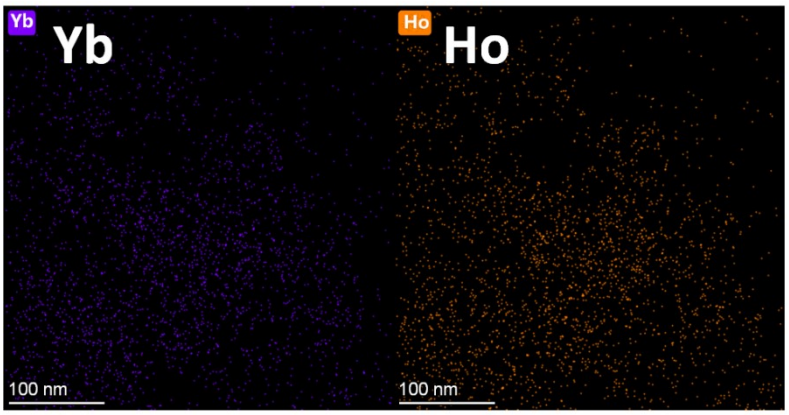

Fig. S2 TEM mapping image of YH-NF/rGO/IS : Yb and Ho.

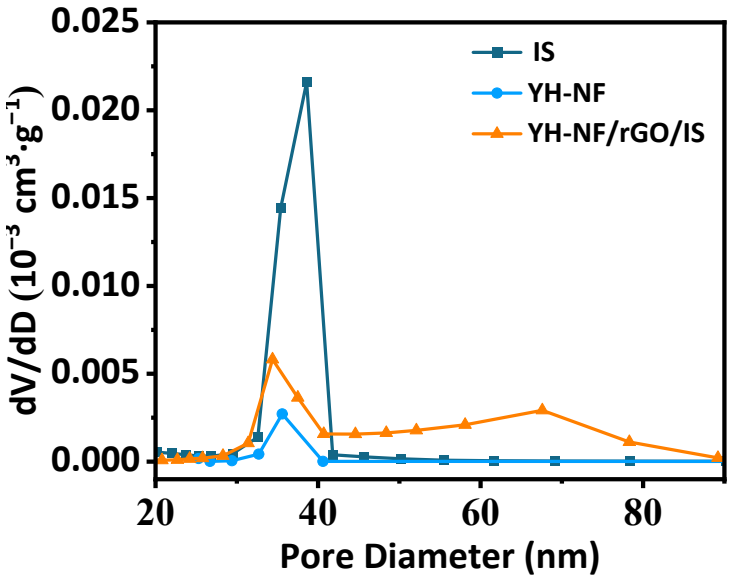

Fig. S3 Pore size distribution of IS, YH-NF and YH-NF/rGO/IS.

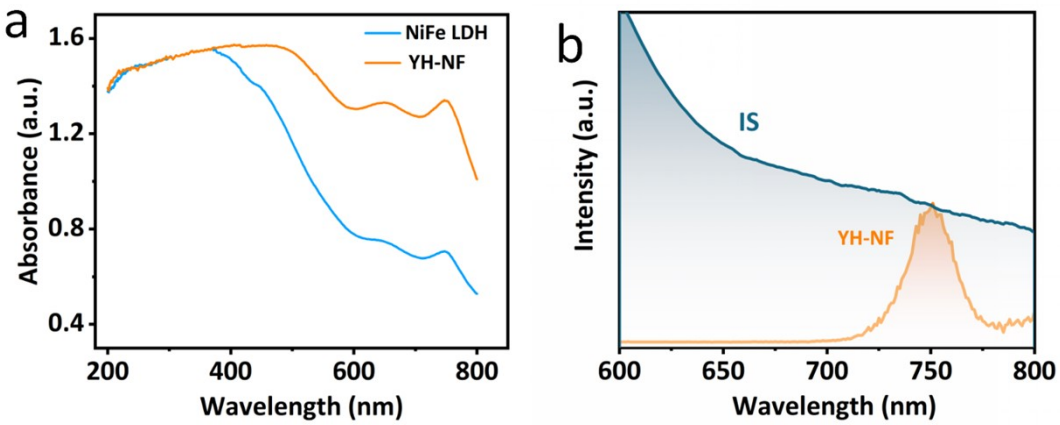

Fig. S4 (a) UV-Vis diffuse reflectance spectrum of NiFe LDH and YH-NF. (b) Overlap region of the absorption spectrum of IS and the UCP spectrum of YH-NF

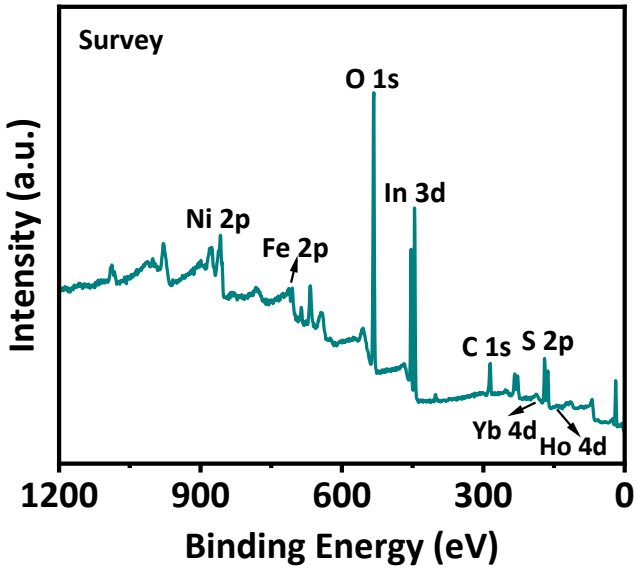

Fig. S5 XPS full spectrum of YH-NF/rGO/IS.

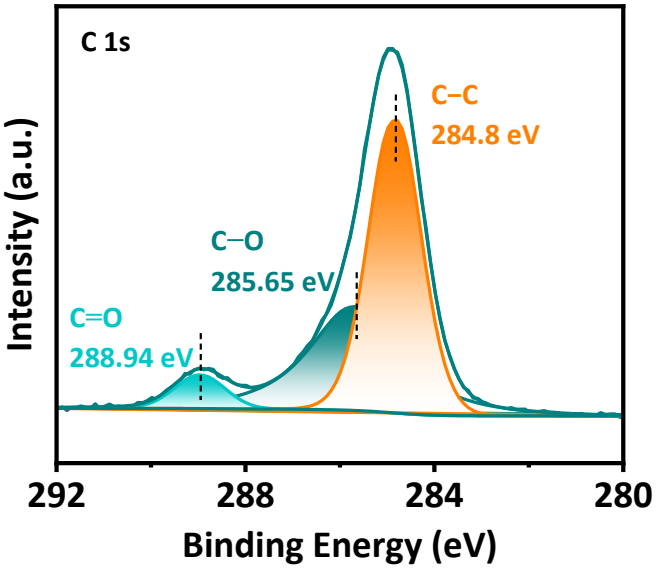

Fig. S6 XPS spectrum of YH-NF/rGO/IS: C 1s.

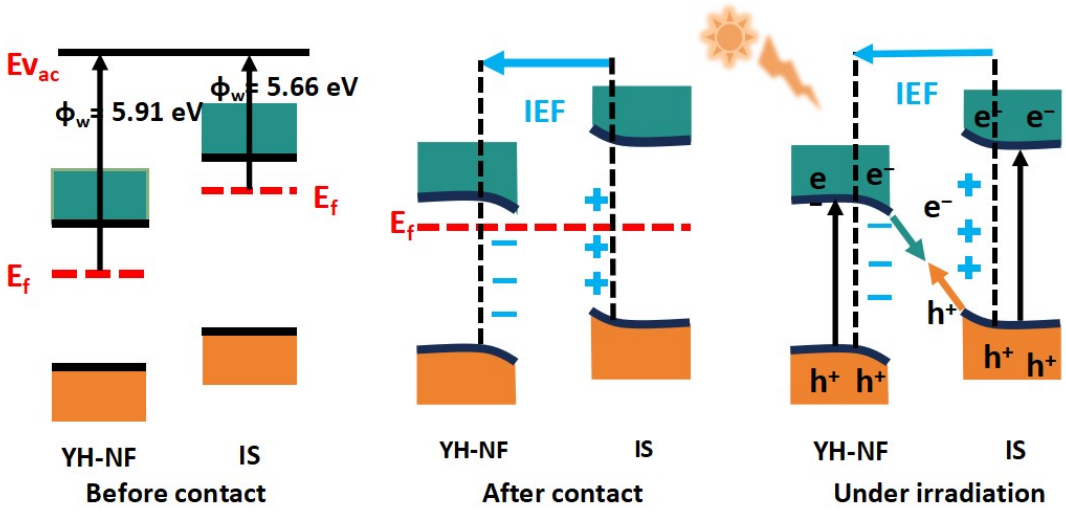

Fig. S7 Schematic diagram of the electron transfer mechanism before and after the contact between YH-NF and IS.

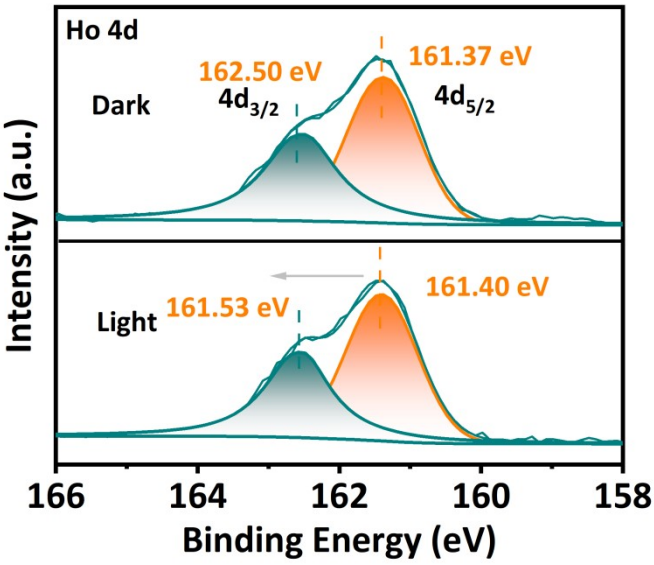

Fig.S8 *In situ* XPS of YH-NF/rGO/IS : Ho 4d.

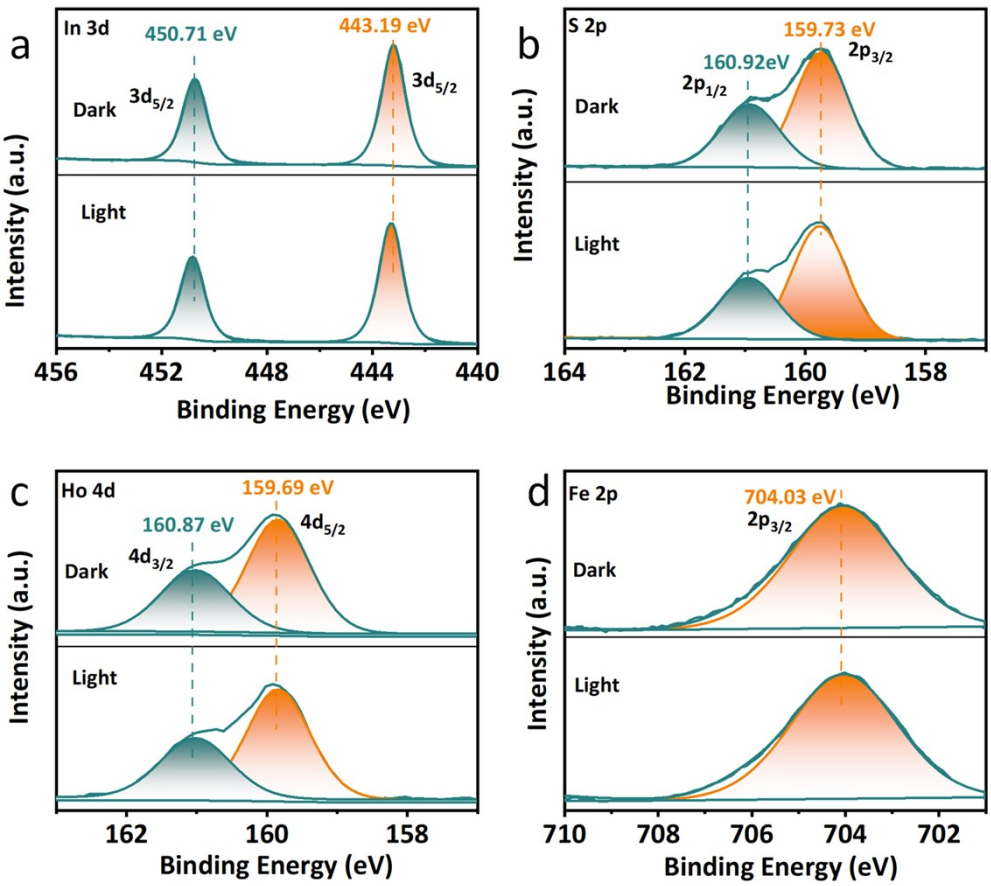

Fig.S9 *In situ* XPS of physical mixture YH-NF/rGO/IS: (a) In 3d; (b) S 2p; (c) Ho 4d and (d) Fe 2p.

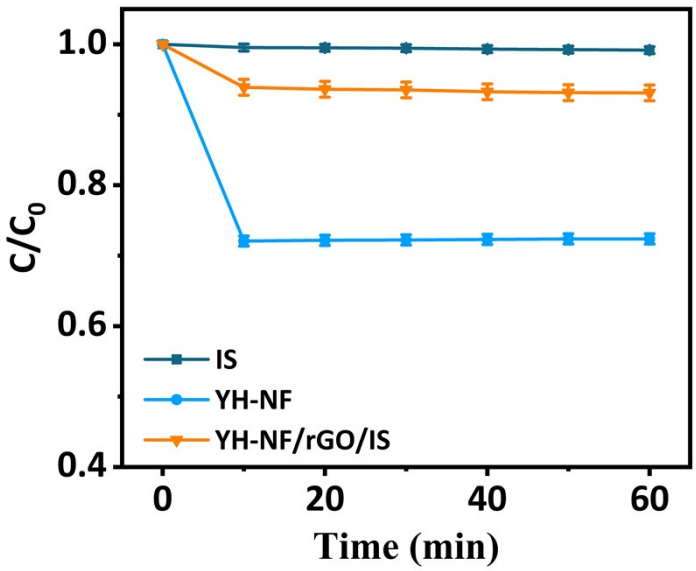

Fig. S10 ONP adsorption curves of IS, YH-NF and YH-NF/rGO/IS in the dark.

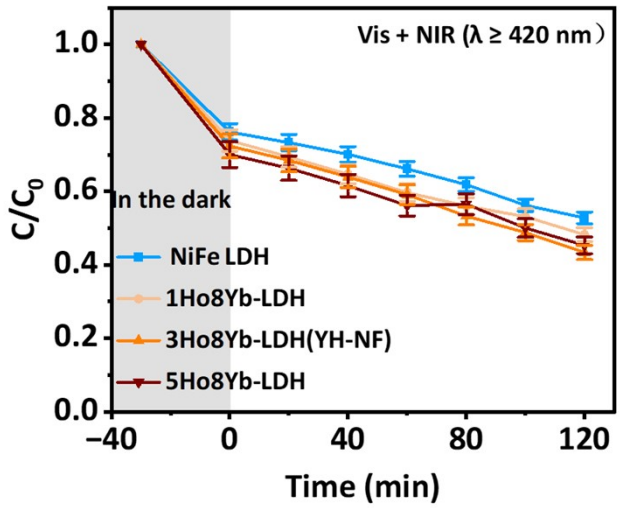

Fig. S11 ONP degradation curves of NiFe LDH with different rare earth doping concentrations under visible light (λ ≥ 420 nm, 555.56 W/m^2).

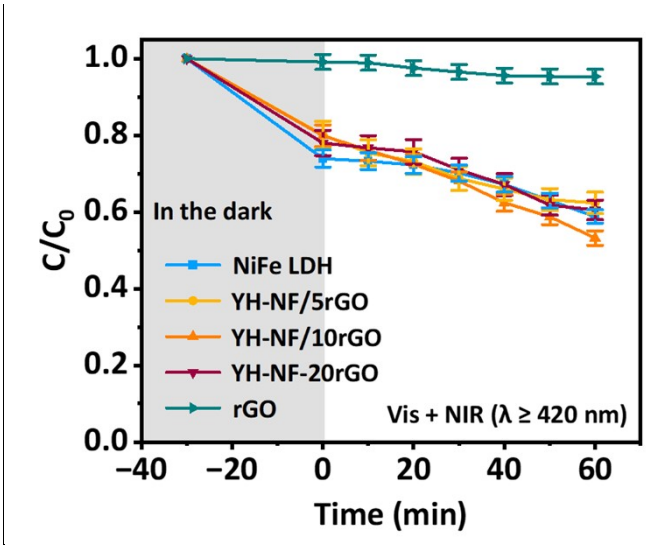

Fig. S12 ONP degradation curves of NiFe LDH with different rGO doping concentrations under visible light (λ ≥ 420 nm, 555.56 W/m^2).

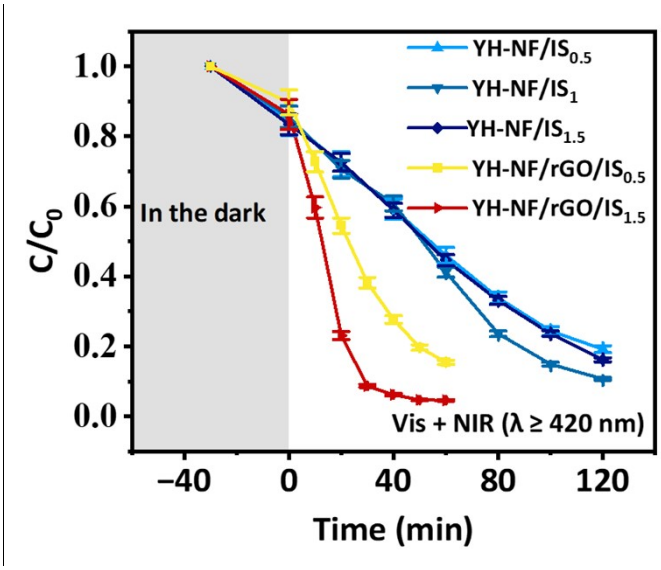

Fig. S13 ONP degradation curves of different samples under visible light (λ ≥ 420 nm, 555.56 W/m^2).

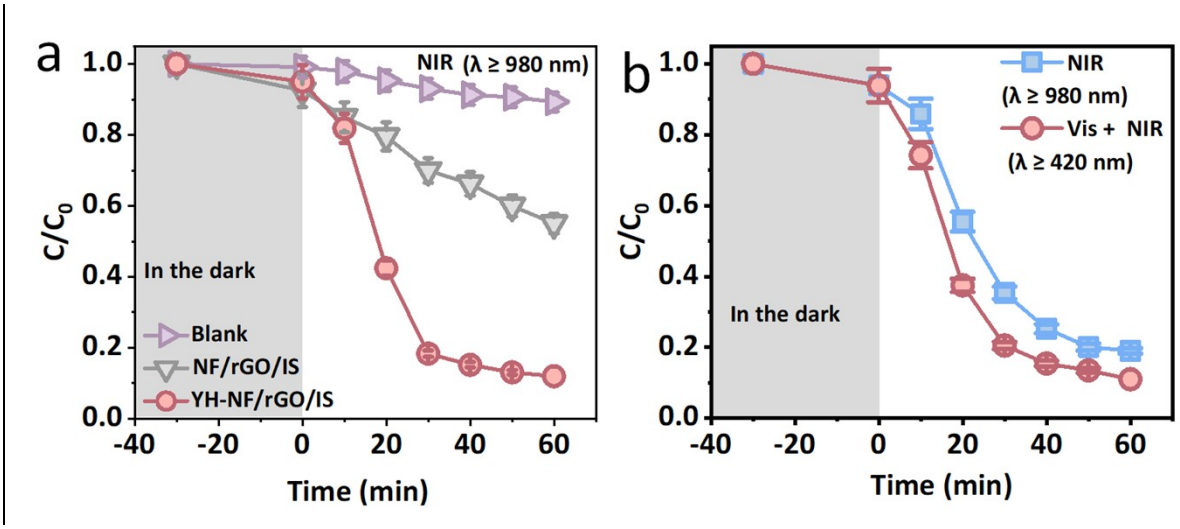

Fig. S14 (a) ONP degradation curves of blank (without samples), NF/rGO/IS and YH-NF/rGO/IS under NIR (λ ≥ 980 nm, 444.45 W/m^2). (b) Degradation curves of ONP by YH-NF/rGO/IS under visible light and NIR light irradiation with same irradiation intensity (370.37 W/m^2).

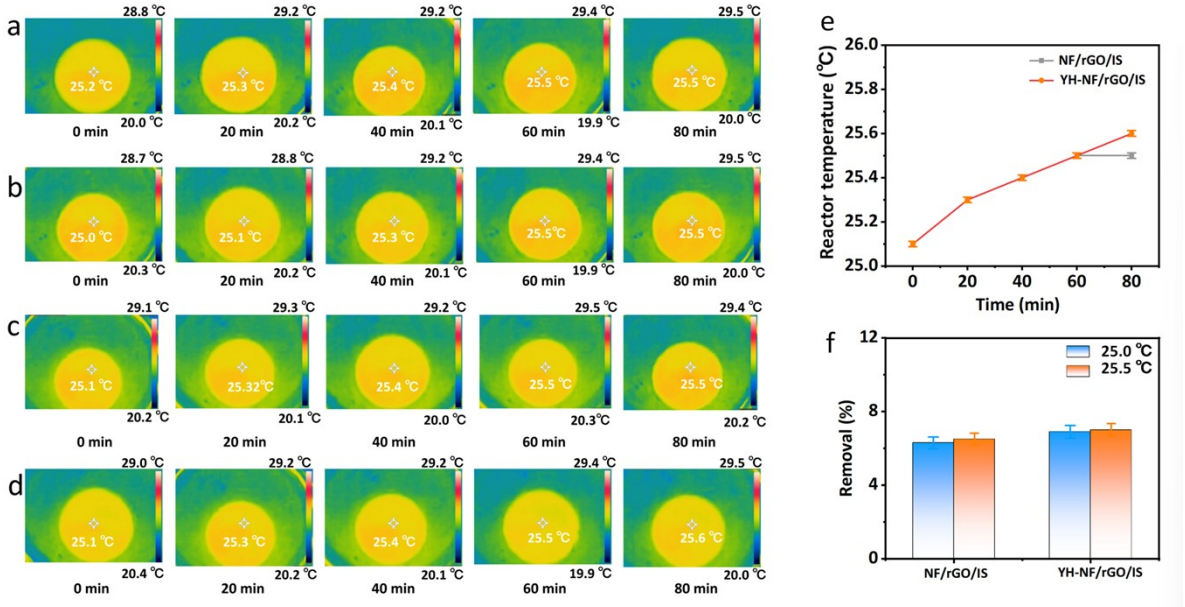

Fig. S15 Reactor temperature *vs* time under NIR illumination over (a) YH-NF, (b) IS, (c) NF/rGO/IS, and (d) YH-NF/rGO/IS; (e) Comparison of react temperature for NF/rGO/IS and YH-NF/rGO/IS; (f) ONP removal of NF/rGO/IS and YH-NF/rGO/IS at 25 °C and 25.5 °C.

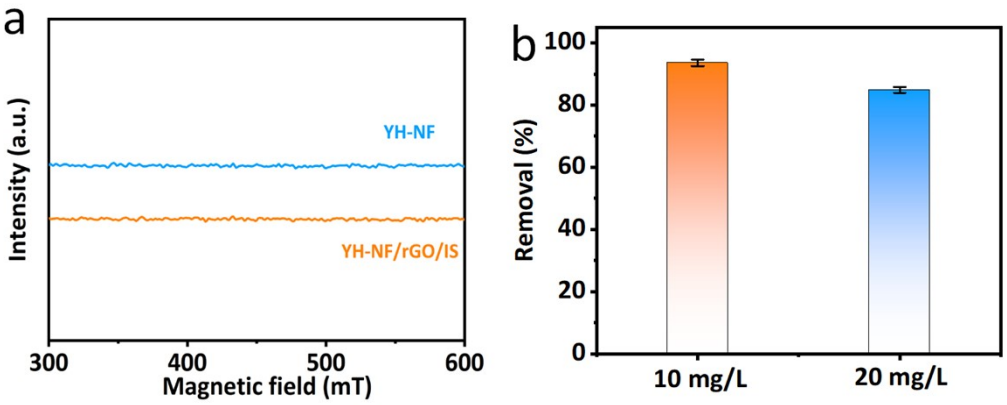

Fig. S16 (a) EPR spectra of YH-NF and YH-NF/rGO/IS; (b) 10 mg/L and 20 mg/L ONP removal of YH-NF/rGO/IS

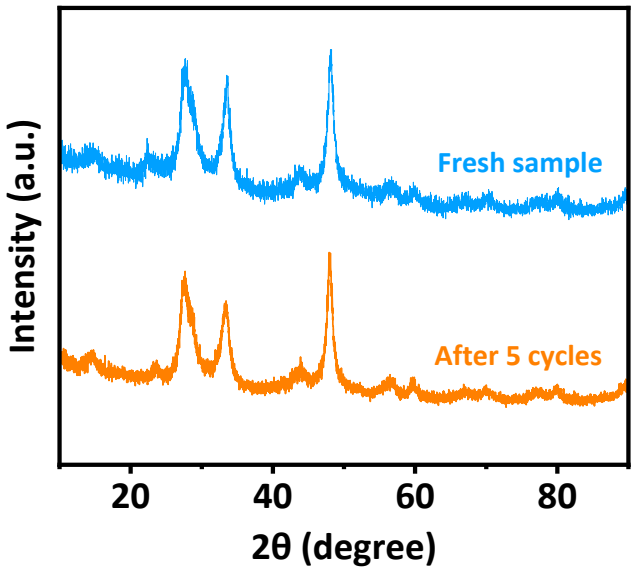

Fig. S17 XRD patterns of YH-NF/rGO/IS before and after cycling

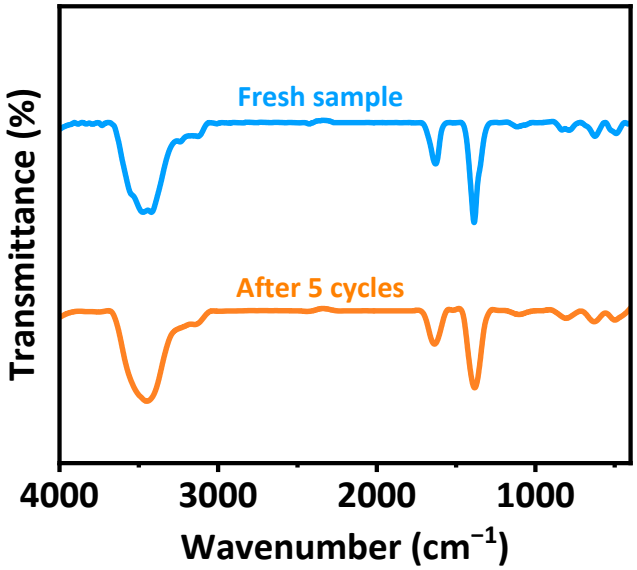

Fig. S18 FT-IR patterns of YH-NF/rGO/IS before and after cycling

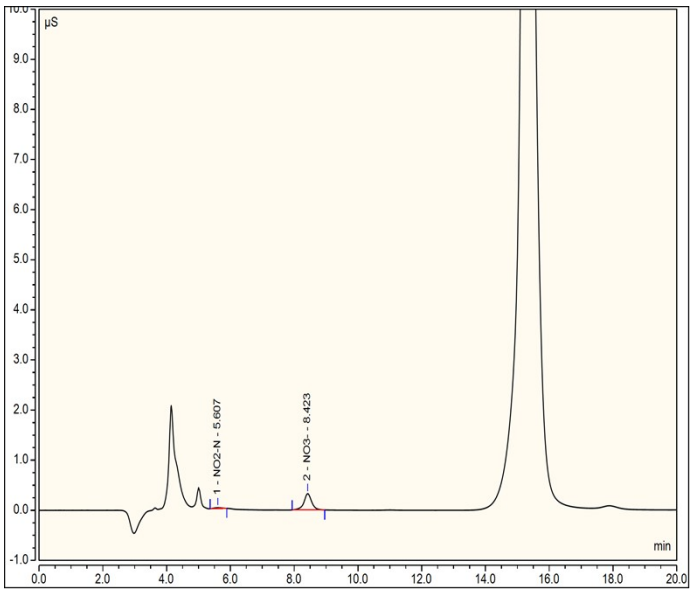

Fig. S19 The nitrate ion chromatography of ONP degradation solution for 100 min after visible light illumination

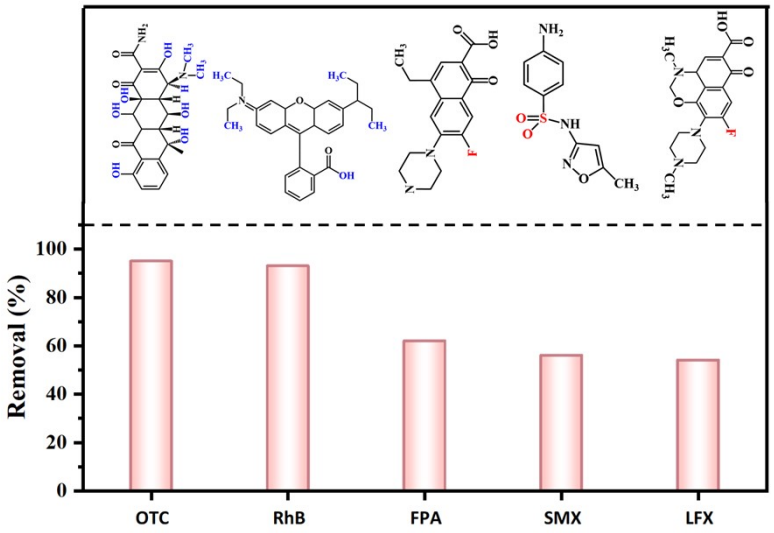

Fig. S20 The degradation curves of YH-NF/rGO/IS for different antibiotic.

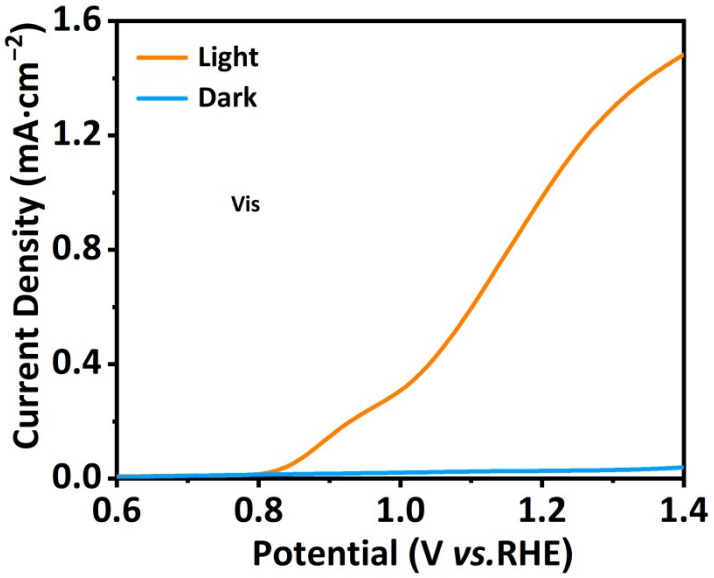

Fig. S21 LSV curves of YH-NF/rGO/IS in the dark and light.

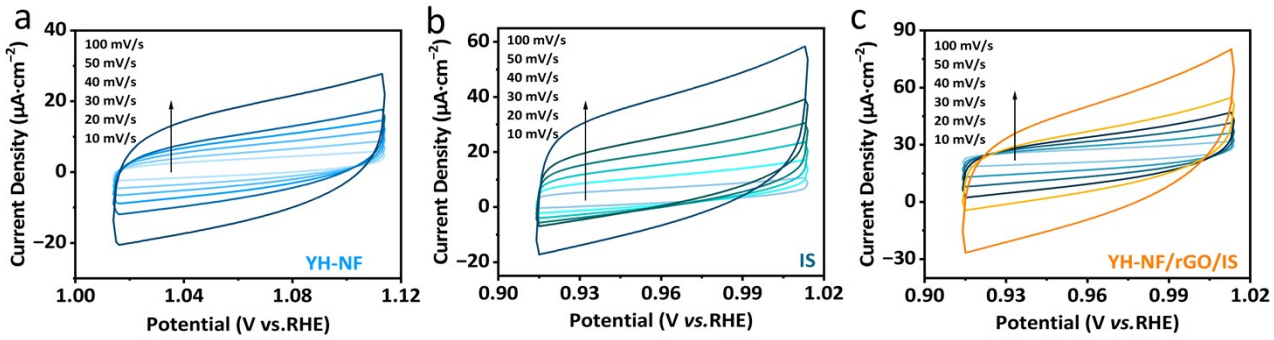

Fig. S22 CV curves of (a) YH-NF, (b) IS and (c) YH-NF/rGO/IS.

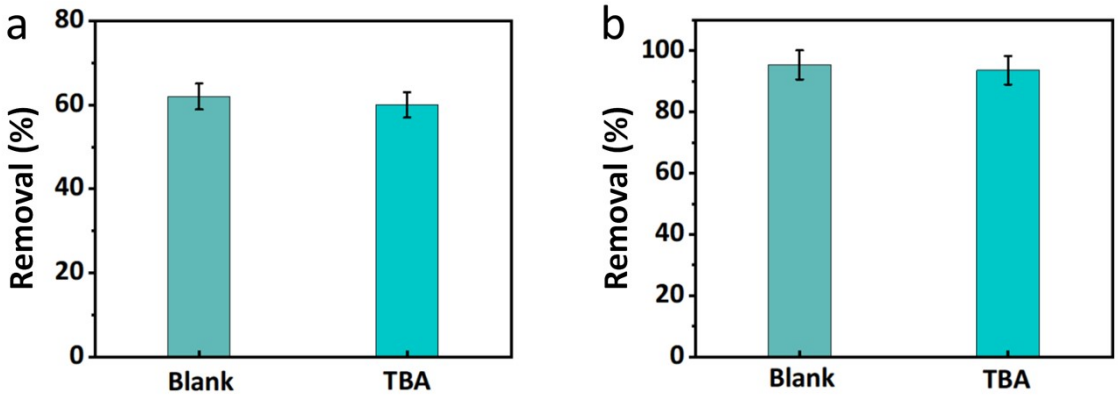

Fig. S23 Scavenger experiments of ·OH (a) YH-NF and (b) YH-NF/rGO/IS.

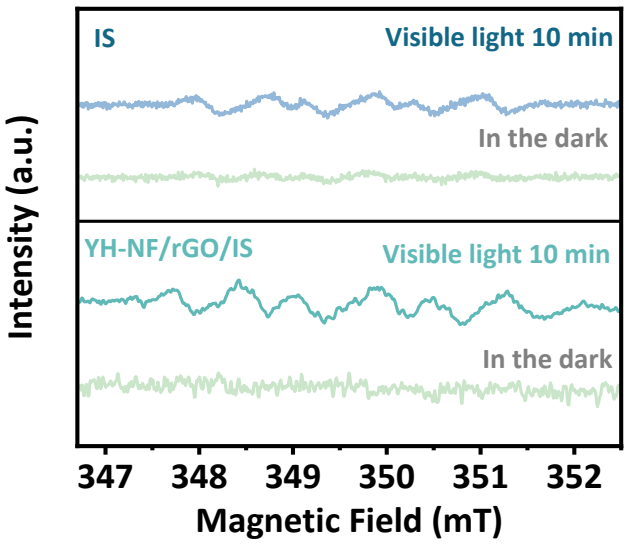

Fig. S24 ESR spectra (DMPO-·O_2^-) of IS, and YH-NF/rGO/IS.

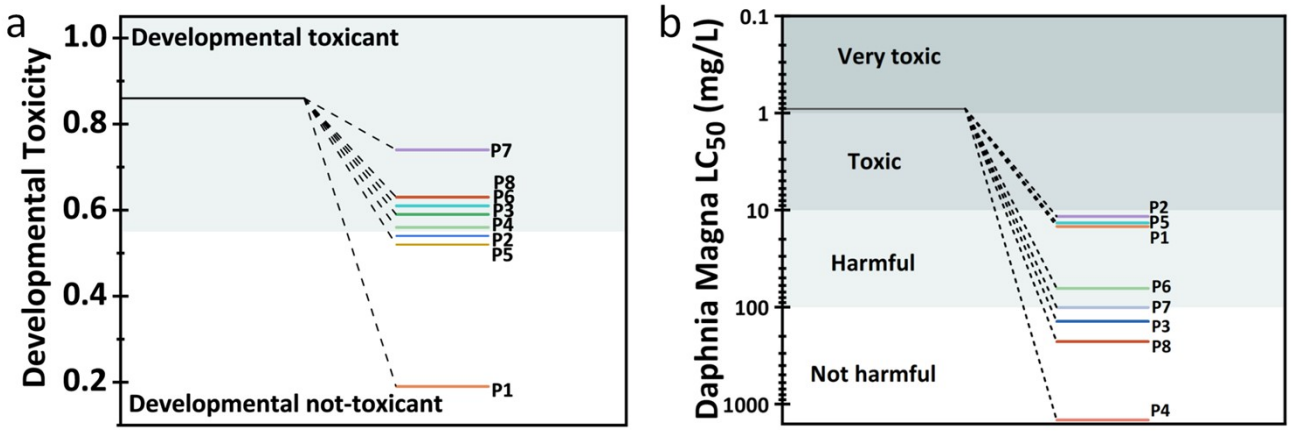

Fig. S25 Development Toxicity (a) and (b) Daphnia magna LC_{50} of the ONP and its intermediates

Section G. Tables

Table S1 BET specific surface area (S_{BET}), average pore size, and pore volume of YH-NF, IS, and YH-NF/rGO/IS_y.

Samples	S_{BET} (m^2/g)	Average pore size (nm)	Pore volume (cm^3/g)
IS	111.93	47.57	0.130
YH-NF	12.35	46.73	0.014
YH-NF/rGO/$IS_{0.5}$	17.09	40.36	0.014
YH-NF/rGO/IS	39.99	51.37	0.017
YH-NF/rGO/$IS_{1.5}$	75.95	71.74	0.046

Table S2 The dosage-dependence study of ONP degradation over YH-NF/rGO/IS.

Dosage (g/L)	Removal (%)	ONP (mg/L)	Time (min)	*k* (min^{-1})	Apparent rate constant ($min^{-1}\cdot g^{-1}$)	R^2
0.2	65.9 ± 1.4	10.0	70.0	0.0087 ± 0.0005	0.0435 ± 0.0028	0.9756
0.3	73.2 ± 1.5	10.0	70.0	0.0120 ± 0.0019	0.0400 ± 0.0063	0.9807
0.4	82.6 ± 1.0	10.0	65.0	0.0280 ± 0.0034	0.0700 ± 0.0085	0.9845
0.5	89.5 ± 1.3	10.0	60.0	0.0380 ± 0.0006	0.0764 ± 0.0130	0.9786
0.6	93.6 ± 1.1	10.0	50.0	0.1750 ± 0.0024	0.2920 ± 0. 0040	0.9820
0.6	84.9 ± 1.2	20.0	70.0	0.0240 ± 0.0029	0.0400 ± 0.0048	0.9812

Table S3 Detected Nitrate ions in the ONP degradation solution for 100 min visible light irradiation.

Peak name	Time (min)	Peak area (μS*min)	Peak height (μS)	Concentration (mg/L)
NO_2^-	5.61	0.005	0.017	0.014
NO_3^-	8.42	0.091	0.327	1.087
	In total	0.10	0.34	1.10

Table S4 LC_{50}, mutagenicity, developmental toxicity of ONP and its intermediates.

Numbers	Mutagenicity	Development Toxicity	Daphnia Magna LC_{50} (mg/L)
P1 (ONP)	0.21 (negative)	0.19	14.67
P2	0.48 (positive)	0.54	11.58
P3	0.20 (negative)	0.59	225.12
P4	0.30 (negative)	0.56	1445.45
P5	0.09 (negative)	0.52	13.51
P6	0.16 (negative)	0.61	63.64
P7	0.32 (negative)	0.74	100.00
P8	0.65 (positive)	0.63	139.55

References：

1 C Zhang, S Hu, W Cui, S Li, L Tian, X Yuan, W Tariq, K Yao, Y Zhi, T Hu, S Shan, Chem. Eng. J, 2025, **510**, 160317.

2 C Liu, S Mao, M Shi, F Wang, M Xia, Q Chen, X Ju, J. Hazard. Mater, 2021, **420**, 126613.

3 Y Lu, Y Cai, S Zhang, L Zhuang, B Hu, S Wang, J Chen, X Wang, Biochar, 2022, **4**(1), 45.

4 Z Meng, J Zhang, H Long, H García, L Zhang, B Zhu, J Yu, Angew Chem Int Ed Engl, 2025, **64**(30), e202505456.

5 P Giannozzi, O Andreussi, T Brumme, O Bunau, M Buongiorno Nardelli, M Calandra, R Car, C Cavazzoni, D Ceresoli, M Cococcioni, N Colonna, I Carnimeo, A Dal Corso, S de Gironcoli, P Delugas, R A DiStasio, A Ferretti, A Floris, G Fratesi, G Fugallo, R Gebauer, U Gerstmann, F Giustino, T Gorni, J Jia, M Kawamura, H Y Ko, A Kokalj, E Küçükbenli, M Lazzeri, M Marsili, N Marzari, F Mauri, N L Nguyen, H V Nguyen, A Otero-de-la-Roza, L Paulatto, S Poncé, D Rocca, R Sabatini, B Santra, M Schlipf, A P Seitsonen, A Smogunov, I Timrov, T Thonhauser, P Umari, N Vast, X Wu, S Baroni, Journal of Physics: Condensed Matter, 2017, **29**(46), 465901.

6 P Giannozzi, S Baroni, N Bonini, M Calandra, R Car, C Cavazzoni, D Ceresoli, G L Chiarotti, M Cococcioni, I Dabo, A Dal Corso, S de Gironcoli, S Fabris, G Fratesi, R Gebauer, U Gerstmann, C Gougoussis, A Kokalj, M Lazzeri, L Martin-Samos, N Marzari, F Mauri, R Mazzarello, S Paolini, A Pasquarello, L Paulatto, C Sbraccia, S Scandolo, G Sclauzero, A P Seitsonen, A Smogunov, P Umari, R M Wentzcovitch, Journal of Physics: Condensed Matter, 2009, **21**(39), 395502.

7 J P Perdew, K Burke, M Ernzerhof, Physical Review Letters, 1996, **77**(18), 3865-3868.

8 J Paier, R Hirschl, M Marsman, G Kresse, The Journal of Chemical Physics, 2005, **122**(23), 234102.

9 S Grimme, S Ehrlich, L Goerigk, Journal of Computational Chemistry, 2011, **32**(7), 1456-1465.

10 S Grimme, J Antony, S Ehrlich, H Krieg, The Journal of Chemical Physics, 2010, **132**(15), 154104.

11 R P Forslund, W G Hardin, X Rong, A M Abakumov, D Filimonov, C T Alexander, J T Mefford, H Iyer, A M Kolpak, K P Johnston, K J Stevenson, Nat. Commun, 2018, **9**(1), 3150.

12 D Lu, L Huang, J Zhang, W Zeng, Q Zhou, ACS Appl. Nano Mater, 2024, **7**(4), 4239-4251.